54th AIAA Aerospace Sciences Meeting/34th ASME Wind Energy Symposium, January 4 - 8 2016, San Diego, CA

Large Eddy Simulation of a 3×3 wind turbine array using Actuator Line model with spectral elements

Tanmoy Chatterjee[*], Yulia Peet[†]

The current paper aims at performing large eddy simulation in spectral element framework of a 3×3 wind turbine array in atmospheric boundary layer (ABL) with near wall modelling for rough-wall geometry at very high Reynolds number. The wind turbine rotors have been represented by state of the art reduced order Actuator Line (AL) model analogous to immersed boundary methodology which is computationally more efficient than resolving turbine blade boundary layer. The inflow condition is fed from an ABL simulation using spectral interpolation method. We present an analysis of multiscale turbulent dynamics and power generated by a 3×3 wind turbine array from the statistical moments and validate the result from experimental observations.

I. Introduction

Wind Energy is one of the rapidly emerging and developing fields of research as a cleaner alternative to energy sources from fossil fuels which are one of the main causes to atmospheric pollution. The harvest of wind power are carried out by large wind farms which are essentially massive arrays of specially arranged wind turbines in atmospheric boundary layer. The fluid dynamics involved in such large wind farms are extremely complex essentially because of the multiscale turbulent transport phenomenon involved past and around the wind turbines in a very high Reynolds number atmospheric boundary layer (ABL) flow. Moreover the turbulent ABL flow intercepted by the wind turbine blades create counter-rotating helical wakes downstream of the turbines which can impinge on other turbines situated in the next row or beyond. These occurrences may adversely affect the extraction of kinetic energy from the wind turbines which have a direct impact on electrical power generation. In the past,[1,2,3] people have studied flow past very large wind farms (streamwise length $L_x \gg 10H$, where H is the BL thickness) using periodic boundary conditions in the streamwise-spanwise direction invoking Wind Turbine Array Boundary Layer (WTABL). This simplified model, does not involve the growth of the inner layer, and allows one to assume the wind turbines as added roughness elements in ABL, without considering many complex phenomenon like wall-bounded turbulence & turbine wake interaction, and wake impingements on turbines at subsequent rows, etc which can be analysed using a simple theory by Frandsen et. al & later extended by Calaf et. al.[4,1,5] Consequently, in order to focus on these phenomenon, we choose to study the dynamic behaviour of the wakes in an isolated 3×3 array of turbines with inflow outflow boundary conditions. Such studies are of great interest not only for rudimentary reasons but also to predict and optimize the performance of wind turbines arranged in a short or intermediate sized wind farms where WTABL assumption fails. Numerical modelling and simulations provide a feasible and accurate way for studying such large-scale turbulence, since direct in-situ or remote sensing experiments can prove to be quite expensive for such kind of study, and it is hard to emulate atmospheric dynamics at laboratory scale measurements within affordable cost.

Nevertheless, flows in the atmospheric boundary layer have very large Reynolds number ($Re \sim 10^8 - 10^{14}$). Using direct numerical simulation (DNS) for such high Reynolds number wall bounded turbulent flow is cost-prohibitive,[6],[7] since capturing all scales of motion in such flows requires computational cost (grid resolution $N_x \times N_y \times N_z \sim O(Re^{2.7})$).[8] In this context, large-eddy simulation (LES) emerged to

---

[*] School for Engineering of Matter, Transport and Energy (SEMTE), Arizona State University; E-mail: tchatte3@asu.edu

[†] Assistant Professor, School for Engineering of Matter, Transport and Energy (SEMTE), Arizona State University; E-mail: ypeet@asu.edu

its immense popularity as it is less cost-intensive than DNS and yet captures the dynamically important, energetic, large-scale structures of certain order $\sim \Delta$ of the flow quite faithfully, while modelling the small scale motions less than Δ having a supposedly universal behaviour.[9,10,11,12] The spatio-temporal evolution of large scales are obtained from spatially filtered Navier-Stokes equations[13,14,15,16] at grid-scale Δ and the subgrid scale (SGS) motions are obtained from the divergence of residual subgrid stress (See section II.A). LES is a promising technique with a potential of generating reliable data of wind turbine simulations not only concerning the flow morphology but also for the power generated by the wind turbines since the "**large-scale structures**" resolved by LES play a pivotal role in the energy output of the turbines. Several attempts at characterizing the performance of wind turbines or wind turbine arrays have been undertaken in the past literature.[17,18,1,19,20]

Additionally, it must be mentioned that resolving the turbine blades boundary layer has the obvious impediments as resolving the atmospheric boundary layer since the chord based Reynolds number would only be an order less in magnitude than the Reynolds number based on Boundary layer thickness. Furthermore, using moving mesh methodology[21] to incorporate the effects of turbine-rotation increases the computational cost significantly beyond two turbines. A reduced-order aerodynamic model analogous to an immersed boundary technique, representing the effect of the rotating blades emerged and later evolved due to the computational bottleneck of fully-resolved calculations[22,23,24,25,18,1,26] (See Ref. 26 for details). The state-of-art model has been first introduced by Sørensen and Shen[25] and later extended by Troldborg[18] in the form of Actuator line (AL) aerodynamics method. The AL model is a fully three-dimensional model which represents the turbine blades (modelled just as rotating 1D lines) with discrete lift, drag and thrust forces emulating the correct rotating effects. The AL method is the most advanced reduced order model till date and has been extensively used in wind turbine array simulations[27] as well as large realistic wind farm simulations.[28,29] The AL model was first extended to and validated in spectral element method by Peet et. al[26] using uniform inflow conditions using Tjærborg turbine. This method was further coupled with a rough wall atmospheric boundary layer model for simulating a single wind turbine case using streamwise periodic boundary condition.[20] In the current paper we propose to perform large eddy simulations of a 3 × 3 wind turbine array in an effort to comprehend the physics of disparate scales of turbulent motion and benchmark the results with experimental observations.[30,31]

The computations on the turbine arrays are performed using a realistic inflow-outflow boundary condition. Various advanced inflow-generation techniques in turbulent boundary layer have been discussed in the literature in the past decade[32,33,34] which were mostly used and validated for smooth wall turbulence with growing boundary layer. For our current simulations with a rough wall model inflow boundary conditions are generated from a separate LES precursor simulation of neutral atmospheric boundary layer (streamwise periodic) at $Re \sim 10^{10}$[20] using standard Smagorinsky eddy viscosity closure in LES with near wall modelling[13,14,12,19] modified for rough wall. The inflow conditions are fed into the wind turbine array domain using a spectral interpolation technique.[21] For the outflow boundary conditions, we have used two different methods, (a) extended a method of Smagorinsky type of non-reflective sponging in our spectral element code for stabilized outflow conditions at a very high Reynolds number[35,36] and (b) a stabilized outflow boundary conditions by Dong et.al[37] and present a comparison on the effect of outflow boundary conditions in the final version of the paper. In the past literature, wind turbine array simulations were mostly performed assuming periodic boundary conditions WTABL with the obvious shortcomings discussed above.[1,5,38] Recently, periodic streamwise boundary conditions with a fringe technique,[39] has also been performed to realistically emulate stabilized inflow-outflow boundary conditions without extention of the domain[40,19] with some works on realistic inflow-outflow boundary conditions on massive wind farms by Churchfield et al.[28,29] The inflow-outflow boundary conditions on a 3 × 3 wind turbine array has the capability of capturing several dynamical phenomenon, e.g. the variation of statistics in the streamwise (flow) direction manifesting the wall turbulence and wind turbine wake interaction, and more importantly, the wake-impingement effects in the second row and beyond, which cannot be captured with WTABL in a periodic box. The analysis of the inflow-outflow turbine array simulations are carried out mostly by studying the first and second order turbulent statistics and also comparing against the results of our most recent WTABL simulation.[3] The development of inflow-outflow boundary conditions in higher order spectral elements retain some novelty from the perspective of its design as are further discussed in Section II.B.2, III.B. In our simulations, we use an open source spectral element code Nek5000[41] featuring superior computational efficiency and parallel performance.

II. Numerical Method

Spectral element code Nek5000[42,43,41] is used to solve the 3D Navier-Stokes (NS) equation for both the actuator line model turbine array and atmospheric boundary layer simulation. Spectral element method (SEM) is a high-order weighted residual technique that combines the geometric flexibility of finite elements with the rapid convergence and tensor-product efficiencies of global spectral methods.
The vectorial form of the unsteady momentum equations coupled with the continuity involves the solution of velocity field $\mathbf{u}(\mathbf{x},t)$ and scalar pressure field $p(\mathbf{x},t)$,

$$\begin{aligned}
\frac{\partial \mathbf{u}}{\partial t} + \mathbf{u}.\nabla\mathbf{u} &= -\frac{1}{\rho}\nabla p + \nu\nabla^2\mathbf{u} + \mathbf{f} \qquad \text{in} \quad \Omega\times(0,T), \\
\nabla.\mathbf{u} &= 0 \quad \text{in} \quad \Omega\times(0,T), \\
\mathbf{u}(\mathbf{x},0) &= \mathbf{u}^0(\mathbf{x}) \quad \text{for} \quad \mathbf{x}\in\Omega, \\
\mathcal{B}(\mathbf{u}_b) &= 0 \qquad\quad \text{in} \quad \partial\Omega.
\end{aligned} \tag{1}$$

Here, $\Omega \subset \mathbb{R}^3$ is the three-dimensional domain in Equation (1), $\mathbf{u}^0(\mathbf{x})$ represents the initial condition of the PDE and $\partial\Omega$ represents the external surface of Ω on which the boundary conditions $\mathbf{u}_b$ are defined. In spectral element methods, the weak formulation of the equations is carried out by weighted residual technique (orthogonal projection of the residual of the equations), or more specifically by Galerkin projection method,[42].[44] The variational formula of the NS equation (used in Nek5000 implementation) can be derived by projecting and minimizing the residual in an orthogonal test space, with test function $\mathbf{v} \in H_1^0(\Omega)^3$.

$$\int_\Omega \mathbf{v}\cdot\frac{\partial\mathbf{u}}{\partial t}\mathrm{d}\Omega + \int_\Omega \mathbf{v}\cdot\mathbf{u}\cdot\nabla\mathbf{u}\mathrm{d}\Omega = -\int_\Omega \mathbf{v}\cdot\nabla p\mathrm{d}\Omega + \frac{1}{Re}\int_\Omega \mathbf{v}\cdot\nabla^2\mathbf{u}\mathrm{d}\Omega + \int_\Omega \mathbf{v}\cdot\mathbf{f}\mathrm{d}\Omega \tag{2}$$

By the choice of v, and simple integration of parts of the pressure and viscous terms it is quite straightforward to see that

$$\int_\Omega \mathbf{v}\cdot(\frac{\partial\mathbf{u}}{\partial t} + \mathbf{u}\cdot\nabla\mathbf{u} - f)\mathrm{d}\Omega = \int_\Omega p\nabla\cdot\mathbf{v}\mathrm{d}\Omega - \frac{1}{Re}\int_\Omega \nabla\mathbf{u}\cdot\nabla\mathbf{v}\mathrm{d}\Omega + \oint_\Gamma(-p + \frac{1}{Re}\nabla\cdot\mathbf{u})\cdot\mathbf{n}\mathrm{d}\Gamma \tag{3}$$

with Γ being boundary condition surface where Dirichlet or periodic boundary conditions are not applied.
In the spectral element formulation the computational domain $\mathbf{\Omega} = \cup_{k=1}^{K}\mathbf{\Omega_k}$. Each $\mathbf{\Omega_k}$ is the image of reference subdomain under a mapping $\mathbf{x}^k(\mathbf{r}) \in \mathbf{\Omega_k} \to \mathbf{r} \in \hat{\mathbf{\Omega}}$, with a well defined inverse $\mathbf{r}^k(\mathbf{x}) \in \hat{\mathbf{\Omega}} \to \mathbf{x} \in \mathbf{\Omega_k}$, where the reference subdomain $\hat{\mathbf{\Omega}} = [-1,1]^d$ with d being the dimension of the problem. Scalar functions with each element $\mathbf{\Omega_k}$ are represented as N^{th} order tensor product polynomials on a reference subdomain $\hat{\mathbf{\Omega}}$. In 3D, any function in the spectral element method in the local element can be expressed as follows

$$f(\mathbf{x})|_{\mathbf{\Omega_k}} = \sum_{m=1}^{N_x}\sum_{n=1}^{N_y}\sum_{p=1}^{N_z} f_{mnp}^k h_m(r_1)h_n(r_2)h_p(r_3), \quad r_1,r_2,r_3 \in [-1,1]^3 \tag{4}$$

where, $h_i(\mathbf{r})$ is the Lagrange polynomial of degree N_x,N_y or N_z satisfying $h_i(\zeta_j) = \delta_{ij}$, where $\zeta = [-1,1]$ and δ_{ij} is the Kronecker delta function. Usually, the polynomial chosen is orthogonal in nature (a solution of Sturm Liouville problem) to obtain least square interpolation error from generalized Fourier series construction. In Nek5000, the orthogonal polynomial used is Legendre polynomial and $\zeta_j, j = 1, N_x$ (for x direction and similarly likewise) are the Gauss-Lobato-Legendre (GLL) points of quadrature. Such choices ensure minimum dissipation and dispersion percolating into the system.
The time discretization of NS solver in Nek5000 involves k^{th} order backward difference/extrapolation scheme (BDF/EXT) where $k = 2$ or 3. The code is fully dealiased using 3/2 rule,[45,46] the velocity is solved using preconditioned conjugate gradient (CG) method and the pressure solver uses iterative generalized mean residual solver (GMRES) method in Krylov subspace. The current algorithm was optimized to achieve perfect scalability in parallel implementation up to 1,000,000 processors.[43,41]

II.A. Large Eddy Simulation

The spatially filtered 3D Navier-Stokes equation for large eddy simulation of wind turbine arrays in neutral ABL flows can be obtained by incorporating a convolution integral filter on the original Navier-Stokes equation

$$\frac{\partial \widetilde{\mathbf{u}}}{\partial t} + \widetilde{\mathbf{u}}\nabla\widetilde{\mathbf{u}} + \frac{1}{\rho}\nabla\widetilde{p^*} - \widetilde{\mathbf{F}} - \nu\nabla^2\widetilde{\mathbf{u}} = -\nabla\cdot\boldsymbol{\tau}(\mathbf{u},\mathbf{u}) \tag{5}$$

The subgrid stress (SGS) tensor in Equation 5, $\boldsymbol{\tau}(\mathbf{u},\mathbf{u}) = \widetilde{\mathbf{u}\mathbf{u}^T} - \widetilde{\mathbf{u}}\widetilde{\mathbf{u}}^T$ arising from the non-commutativity of filtering with the nonlinear advection term, is modelled using a Smagorinsky type eddy viscosity closure. The model SGS stress $\boldsymbol{\tau}^{SGS}(\widetilde{\mathbf{u}},\widetilde{\mathbf{u}})$ can be given as $\boldsymbol{\tau}^{SGS} - \frac{1}{3}tr(\boldsymbol{\tau}^{SGS})\mathbb{I} = -2\nu_t\nabla^s\widetilde{\mathbf{u}}$. In classical Smagorinsky model, $\nu_t = (l_f)^2|\nabla^s\widetilde{\mathbf{u}}|$, with filter length scale $l_f = C_s\Delta$,[47] Δ is a grid scale and the term $|\nabla^s\widetilde{\mathbf{u}}|$ can be given as $|\nabla^s\widetilde{\mathbf{u}}|^2 = 2\nabla^s\widetilde{\mathbf{u}} : \nabla^s\widetilde{\mathbf{u}}$ and $\nabla^s\widetilde{\mathbf{u}} = \frac{1}{2}(\nabla\widetilde{\mathbf{u}} + \nabla\widetilde{\mathbf{u}}^T)$. For high Reynolds number turbulent ABL flow, we employ the algebraic wall damping by Mason and Thompson (1992),[47]

$$\frac{1}{l_f^n} = \frac{1}{(C_0\Delta)^n} + \frac{1}{\kappa(z+z_0)^n} \quad z_0 \ll H. \tag{6}$$

For best results in our SEM model (see [20] for details), the ad-hoc blending function parameters $C_0 = 0.19,\ n = 0.5$.

The forcing term $\widetilde{\mathbf{F}}$ in the neutral ABL represents the mean streamwise pressure gradient that drives the flow, while in actuator line model it represents the thrust, lift and drag forces experienced by the fluid through the actuator lines.

II.B. Boundary Conditions

II.B.1. Neutral Atmospheric Boundary layer: Realistic Inflow

We incorporate periodic boundary conditions in the streamwise and spanwise direction while the top boundary conditions are stress free: $d\widetilde{u}/dz = d\widetilde{v}/dz = 0$, and $\widetilde{w} = 0$ (x: streamwise direction, y: spanwise direction and z: wall normal direction). At the bottom surface, we use a wall stress boundary condition without having to resolve the rough wall, relating the wall stress vector to the horizontal velocity vector $\widetilde{\boldsymbol{u}_h}$ at the first grid-point using the standard Monin-Obukhov similarity law[48] along with no-penetration conditions of large eddies, $\widetilde{w} = 0$.

$$\frac{1}{\rho}\boldsymbol{\tau}_s = -\kappa^2 \frac{\widehat{\widetilde{\boldsymbol{u}}}_{h,\frac{\Delta z}{2}}(x,y,t)|\,\widehat{\widetilde{\boldsymbol{u}}}_{h,\frac{\Delta z}{2}}|(x,y,t)}{\log(\frac{z}{z_0})\Big|^2_{\frac{\Delta z}{2}}} \tag{7}$$

where, $|\,\widehat{\widetilde{\boldsymbol{u}}}_{h,\frac{\Delta z}{2}}| = \sqrt{\widehat{\widetilde{u}}^2_{\frac{\Delta z}{2}} + \widehat{\widetilde{v}}^2_{\frac{\Delta z}{2}}}$ and $\widehat{\widetilde{\boldsymbol{u}}}_{h,\frac{\Delta z}{2}} = \widehat{\widetilde{u}}_{\frac{\Delta z}{2}}\vec{e_x} + \widehat{\widetilde{v}}_{\frac{\Delta z}{2}}\vec{e_y}$ ($\vec{e_x}, \vec{e_y}$ are unit vectors in the x, y direction). The "hat" represents additional explicit filtering carried out in the modal space by attenuating $k_c = 4$, highest Legendre polynomial modes of the spectral element model.[20] For collocated spectral element methods $\widehat{\widetilde{u}}_{\frac{\Delta z}{2}}$, $\widehat{\widetilde{v}}_{\frac{\Delta z}{2}}$ are calculated as an interpolation at half wall node $\Delta z/2$ e.g., between $\widehat{\widetilde{u}}(x,y,0,t)$ and $\widehat{\widetilde{u}}(x,y,z=\Delta z,t)$, (and similar procedure for $\widehat{\widetilde{v}}$) where Δz is the first GLL grid point from the wall. A proper choice of the subgrid scale model with wall damping used in LES simulations with near wall modelling is essential, since the proper dissipation characteristics of the SGS model generate accurate subgrid scale stresses and kinetic energy which is necessary for generating the log-law profile and correct second order statistics near the wall.[49, 12, 50]

II.B.2. Wind Turbine Array

The boundary conditions for the rectangular domain of wind turbine array are very similar to the ABL domain (spanwise periodic, symmetry at the top and shear stress at the bottom "wall"), except for the streamwise direction where we choose to use a realistic inflow-outflow condition. The inflow condition is turbulent in nature and to maintain a realistic spatio-temporal coherence the inflow is being fed from a separate precursor ABL simulation. The choice of outflow boundary conditions in our spectral element code requires a careful analysis. Invoking Equation 3 we see that the simplest choice of natural "do nothing" boundary condition at the outflow would be

$$(-p + \frac{1}{Re}\nabla\cdot\mathbf{u})\cdot\mathbf{n} = 0 \quad \text{on} \quad \Gamma \tag{8}$$

However implementing such boundary conditions at high Reynolds number triggers amplification of outgoing large eddy structures at the outflow resulting in reflection and instability. To circumvent this problem we have used sponging by extending the domain with coarse elements and adding sufficient amount of artificial viscosity near the outflow region ensuring required dampening of the eddies before they go to the outflow boundary. However, sudden change in viscosity in the interface of physical and extended domain can be dangerous giving rise to spurious reflective waves which can potentially trigger instability. Consequently, we have extended the idea of carefully-designed non reflective sponging layer using simple Smagorinsky type viscosity in the sponge layer which restricts the indiscriminate growth of viscosity in that region. In the sponge-layer, $\nu = \nu_m + \nu_{sl}$, with ν_m being the molecular viscosity where $\nu_{sl} = (C_{sl}\Delta)^2|\widetilde{S}|$, with $|\widetilde{S}| = \sqrt{2\widetilde{S}_{ij}\widetilde{S}_{ij}}$. Δ is metric of grid spacing scale which is similar to that in LES Smagorinsky model.[20] In our spectral element model C_{sl} is designed to grow quadratically in the form $C_{sl} = b(x - x_0)^2$, with $b = 0.25$ and x_0 is the end of the streamwise extent of physical domain. The natural boundary condition with a non-reflective sponge layer is seen to stabilize eddies at the outflow. Additionally, we have also used a superior a more accurate stabilized natural boundary conditions by Dong et. al[37] which can be given as

$$-p \cdot \mathbf{n} + \frac{1}{Re}\nabla\mathbf{u} \cdot \mathbf{n} - \frac{1}{2}|\mathbf{u}|^2\Theta(\mathbf{n}, \mathbf{u}) = 0 \text{ on } \Gamma \tag{9}$$

where

$$\Theta(\mathbf{n}, \mathbf{u}) = \left(1 - \frac{\tanh(\mathbf{n} \cdot \mathbf{u})}{U\delta}\right)$$

is smooth Heaviside step function to remove sudden discontinuity of the outflow fluxes with U, δ being some chosen velocity and length scale in the flow and $\mathbf{n}$ is the unit normal vector at the outflow boundary. This boundary condition has been tested to stabilize energy of the system $1/2||\mathbf{u}||^2_{L_2(\Omega)}$ (projecting NS equation with $\mathbf{u}$) compared to a simple natural boundary condition[51] (See Equation 8). Unless otherwise mentioned, all the results of our simulation presented in this paper involve the second outflow boundary condition and a comparison of the two different outflow boundary conditions are also reported.

II.C. Actuator Line Model: Turbine Response

In an actuator line model,[18] the blades are divided into elements, similar to BEM, and the local lift (L) and drag (D) force experienced by each element is calculated as $(L\ ,\ D) = \frac{1}{2}C_{(l,d)}(\alpha)\,\rho\,V_{rel}^2\,c\,w_d$ where c is the chord length and w_d is the blade thickness. The local aerodynamic force $\vec{f} = L\vec{e_L} + D\vec{e_D}$ (here $\vec{e_L}$ and $\vec{e_D}$ are the unit vectors in the direction of the local lift and drag, respectively) can be calculated by computing angle of attack α from V_{rel}, streamwise velocity V_x and pitch-angle γ (Figure 1). The total reaction force from all the blade elements experienced by the fluid distributed smoothly on several mesh points is given by

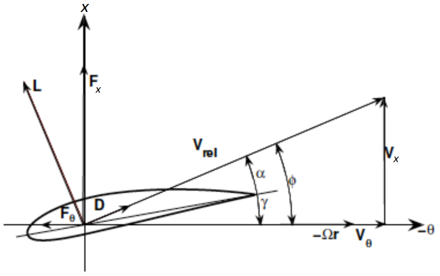

Figure 1: Velocity triangle for the determination of the local relative velocity on a turbine blade.

$$\vec{F}(x,\, y,\, z,\, t) = -\sum_{i=1}^{N} \vec{f}(x_i,\, y_i,\, z_i,\, t)\, \eta_\epsilon(|\vec{r} - \vec{r_i}|), \tag{10}$$

using a smeared out delta function in the form of a Gaussian $\eta_\epsilon(d) = 1/\epsilon^3\pi^{3/2}\exp\left[-\left(d/\epsilon\right)^2\right]$. The summation in the forces is over all N blade elements, and $\epsilon = 2\,w_d$ is used in the current study. The AL model is more advanced than the actuator-disc model[52, 1] commonly used in numerical computations of WTABL, in its capability to capture the tip-vortices being shed in the near-wake quite accurately.[18, 20]

III. Computational Setup

III.A. Neutral Atmospheric Boundary layer simulations

The computational domain of the neutral ABL simulation is of rectangular geometry and cartesian spectral element collocated mesh has been used for such calculations. We model a similar setup as in Ref. 12 for neutral ABL simulations. In the present cartesian framework, x is the streamwise direction, y is the spanwise direction and z is wall normal direction. The computational domain for the ABL simulations is $2\pi H \times \pi H \times H$, where $L_x = 2\pi H$, $L_y = \pi H$, and $L_z = H$ is the boundary-layer thickness. The domain is uniformly discretized into $30 \times 20 \times 24$ elements in $x, y,$ and z directions respectively. With 8^3 GLL points per element, the number of grid points for the ABL simulations is $211 \times 141 \times 169 \approx 5 \times 10^6$. The rough wall closure and subgrid scale (SGS) eddy-viscosity models used for the large eddy simulations of ABL model are described in Sections II.B.1, II.A respectively. The discretization parameters of the domains are tabulated below. Table 1 clearly reveals the anisotropy of the streamwise grids ($\Delta_x/\Delta_z,\ \Delta_x/\Delta_z$) with respect to the wall normal and spanwise grid in the near wall region which conforms well with the past literature.[7,50] N_i^e represents the number of elements in the i^{th} direction while $\Delta_x,\ \Delta_y,\ \Delta_z$ are the minimum grid sizes of the GLL nodes within each element. $\Delta z/z_0 \gtrapprox 25$ ($z_0 = 10^{-4}H$) manifesting the first grid node does not resolve the geometric roughness and lies in the log-law of the wall.

Geometry	$N_x^e \times N_y^e \times N_z^e$	Δ_x/Δ_z	Δ_x/Δ_y	$\Delta z/z_0$
$2\pi H \times \pi H \times H$	$30 \times 20 \times 24$	4.98	4.11	27.88

Table 1: Numerical setup for neutral ABL flow LES. GLL nodes 8 per cartesian direction.

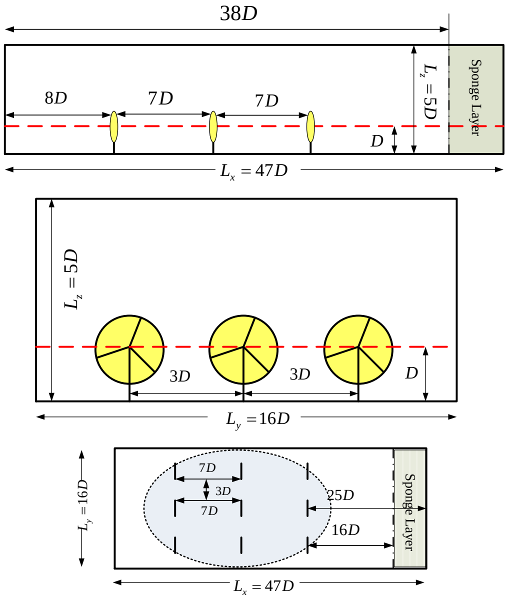

Figure 2: Computational domain of wind turbine array AL simulations. top: $x - z$ plane, middle:$y - z$ plane, bottom: $x - y$ plane. The red-dashed line represents the hub-height of the rotors; the dotted ellipse in the bottom figure represents the region of 3×3 wind turbine array

III.B. Actuator Line Simulation of Wind turbine array

The domain size for the actuator line model wind turbine array is $3\pi H \times \pi H \times H$, with the statistically stationary ABL simulation serving as an initial condition to the actuator line model. Consequently, a seperate ABL simulation at that domain length has been run with a uniform discretization of $40 \times 24 \times 20$ elements to generate realistic initial conditions for turbine array simulations. The domain size rescaled in terms of turbine rotor radius (diameter) is given as $94R \times 32R \times 10R$ ($47D \times 16D \times 5D$), where $R = 0.1H$ is the radius of each turbine-rotor ($D = 2R$ is turbine-rotor diameter). The hub-height of all the turbines are at $z_h = D$. The 9 turbine rotors have been arranged in a 3×3 matrix arrangement in the computational domain. The design of the computational domain and the arrangement of different turbines are done in concordance with the experimental set up as in Ref. [2,30] (See Figure 2). The first row of 3 rotors are placed at $\pi H/2$ or $8D$ distance from the inflow boundary. The streamwise distance between the turbines is $7D$, while the spanwise distance is $3D$. The hub-height of all the rotors have been set at D. These dimensions are designed to conform the experimental set-up as in Ref. [38,30]. The physical streamwise extent of the domain is $38D$, after which the non-reflective sponge layer initiates with a coarse 2 element stretch to $x = 47D$ coupled with natural outflow boundary condition (See Equation 8). However, for implementing stabilized natural boundary condition,[37] it was observed in the previous literature as in Ref. 51 that extended domains are still required such that the stabilized boundary conditions do not affect eddies upstream in the flow. The turbulent inflow conditions are implemented as a stationary overlapping mesh methodology,[21] where both the simulations are run simultaneously with the inflow condition from ABL simulation being generated by spectrally interpolating the mid-plane of the ABL domain (yz plane at $x = \pi H$) to the inflow boundary of the computational domain of turbine array (direct memory copies). Since, the spectral interpolation is done in parallel using Message Passing Interface (MPI) it removes the I/O overhead significantly in the computation. The details of the different parameters like tip-speed ratio, chord length, lift and drag coefficients pertaining to turbine blades used in the current simulation can be found in Chatterjee and Peet.[20] The drag forces experienced by the cylindrical nacelle has been modelled by using a simple model using $F_{drag} = \frac{1}{2} C_D \rho U_{bulk}^2 A$, with $C_D \sim 0.9$ and A being the cross-sectional area for the nacelle in the current simulations. The subgrid scale model remains the same as in ABL simulations (See Section II.A).

Case	Geometry	$N_x^e \times N_y^e \times N_z^e$	Grid points
Sponge Layer	$3\pi H \times \pi H \times H$	$42 \times 32 \times 24$	1.122×10^7
Stabilized NBC (Dong et. al)	$3\pi H \times \pi H \times H$	$48 \times 32 \times 24$	1.281×10^7

Table 2: Numerical setup for wind turbine array computational domain for two different outflow boundaries. 8 GLL nodes has been used per cartesian direction

IV. Results

IV.A. Validation

Figure 3 shows benchmark statistic and spectra results of our current LES simulation of neutral ABL flows. In absence of near-wall unphysical subgrid scale dissipation ($C_0 = 0.19,\ n = 0.5$) the mean-stream wise velocity gradient $\kappa z/u_\tau dU/dz$ in Figure 3a shows excellent logarithmic trends ($\phi(z) = 1$) in the inner layer $z/H \lesssim 0.1$. The current LES model captures the k_x^{-1} and $k_x^{-5/3}$ law corresponding to the double overlap region of streamwise velocity spectra $E_{uu}(k_x)$ and the Kolomogorov $-5/3$ law of the wall normal velocity spectra $E_{ww}(k_x)$[55,56] quite successfully as shown in Figures 3b, 3c.

Before moving on with the discussion of an isolated 3×3 wind turbine array, we also discuss some results of a periodic wind turbine array (WTABL). This is done in an effort to validate our code with standardized benchmarks and also reveal the limited capability of the model in capturing the dynamics of a large wind farms. In a WTABL, the wind turbine arrays essentially act as an additional imposed roughness to the neutral atmospheric boundary layer. This is manifested in a double equilibrium log-layer in Figure 4a. The lower log-law with friction velocity $u_{*,lo}$ and roughness height $z_{0,lo}$ corresponds to the attached eddy layer due to imposed bottom wall roughness, while the upper log-law with $u_{*,hi}, z_{0,hi}$ comes from the “wind-turbine roughness”.[1] Figure 4b shows the turbulent shear stress flux (Reynolds and dispersive stresses, See[1] for details) the downward entrainment (difference of fluxes at $z_h \pm D/2$, where $z_h = D$ is the hub-height) of which contributes to the turbine power generation. The LES simulations of both the WTABL model as well as the isolated wind turbine array (Figure 5) depicts the large scale structures on or around the turbines in the computational domain. For details of the periodic WTABL simulation refer to.[3]

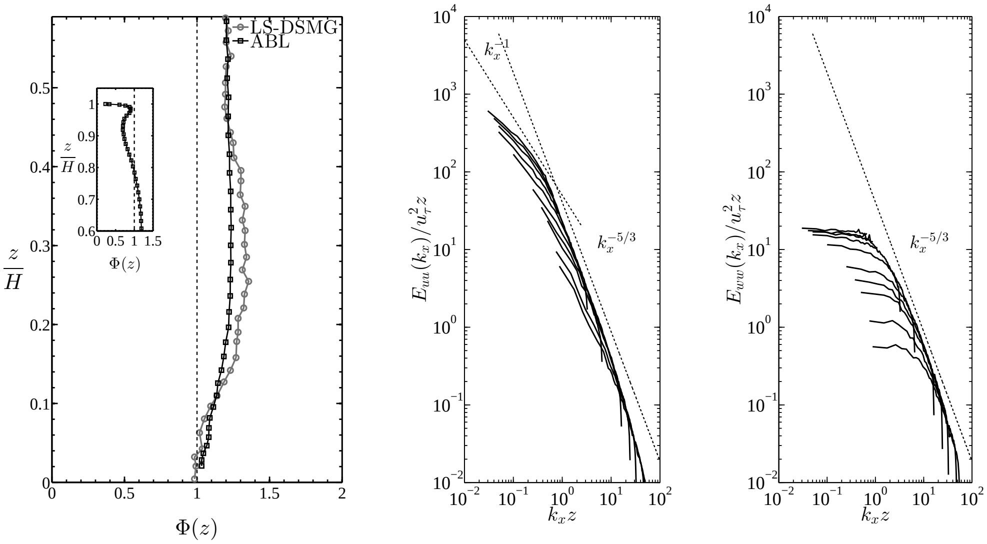

(a) (b) (c)

Figure 3: (a)Variation of non-dimensional velocity gradient $\phi(z) = \kappa z/u_\tau dU/dz$ vs z/H, LS-DSMG: Lagrangian scale dependant SGS model, Bou-Zeid et al.[57] ABL: Current LES simulation of neutral ABL (b) Streamwise (c) Wall normal Energy spectra ($E_{uu}(k_x)$, $E_{ww}(k_x)$ respectively) vs normalized streamwise wavenumber $k_x z$ for neutral ABL. u_τ is the bottom “wall” friction velocity scale.

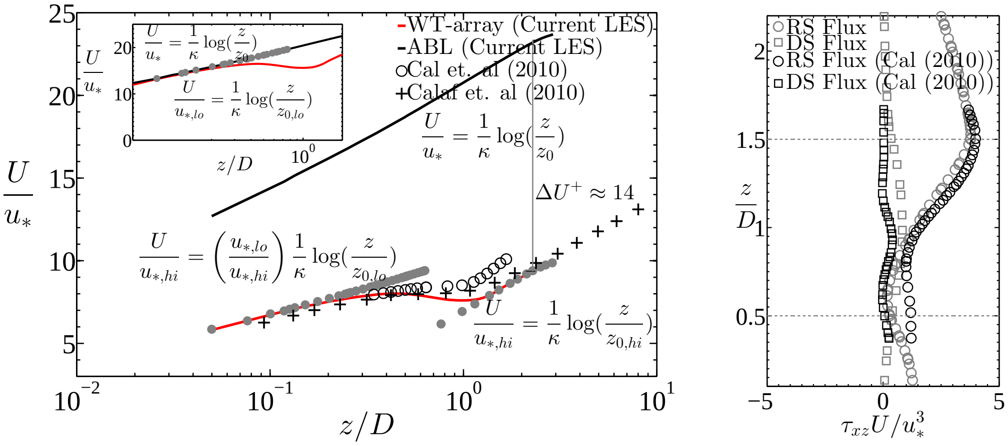

(a) (b)

Figure 4: WTABL Simulation with streamwise-spanwise periodicity (a) Double Log law trends of mean streamwise velocity (b) Turbulent shear stress flux of mean kinetic energy, Reynolds and Dispersive Stress contribution. $z = D$ is the hub-height location. Figures taken from .[3]

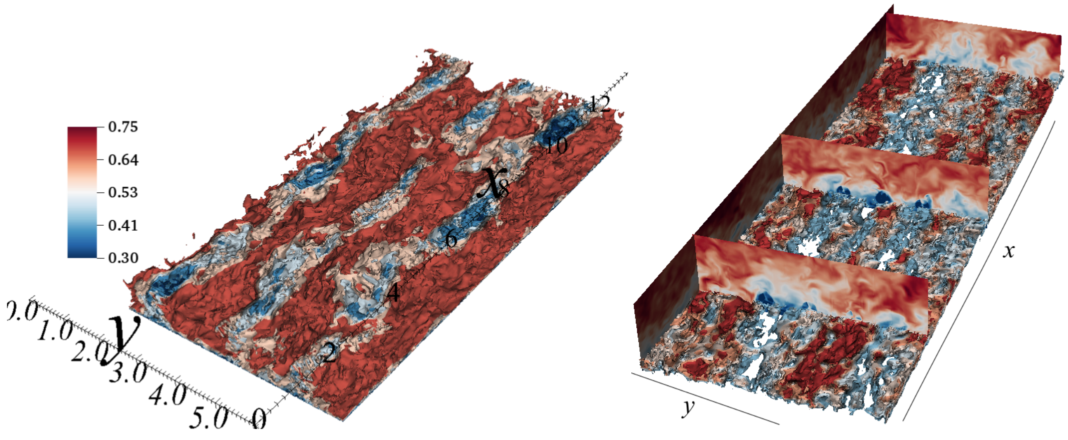

(a) (b)

Figure 5: Large scale eddies: Iso surfaces of velocity magnitude (a) WTABL, periodic domain (b) 3 × 3 isolated wind turbine array

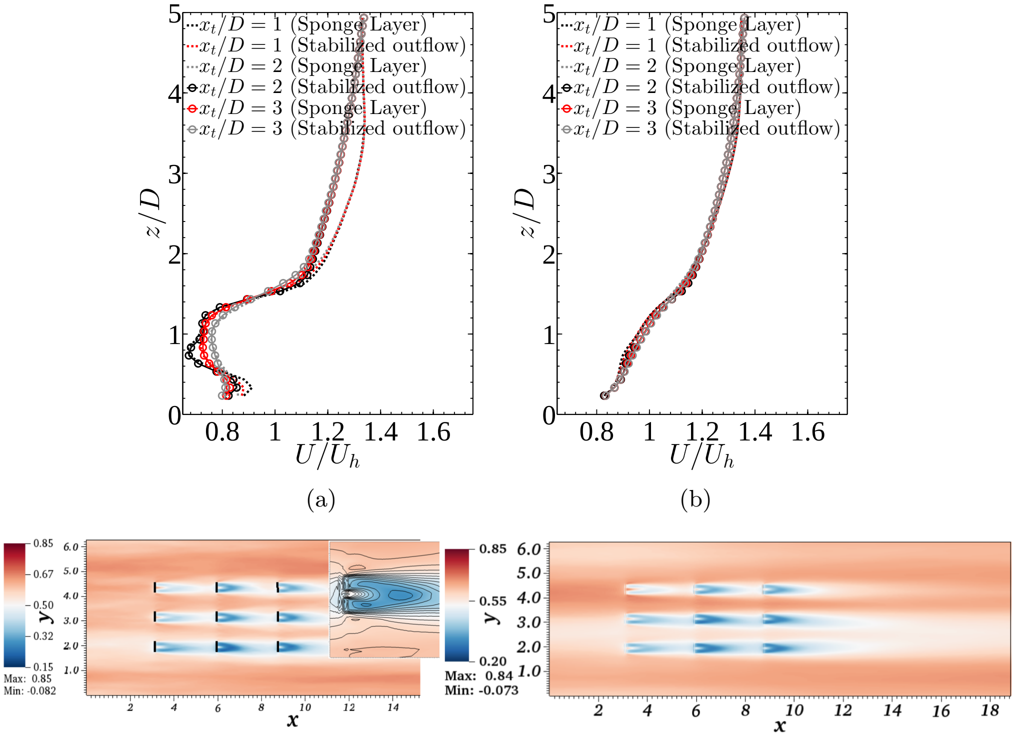

(a) (b)

(c) (d)

Figure 6: Comparison of two differnt outflow boundary conditions. Temporally averaged mean streamwise velocity (a) spanwise averaged over one turbine disc (b) spanwise averaged over the entire domain. Streamwise average velocity contour in xy plane (a) Sponge Layer (b) Stabilized natural outflow boundary conditions[37]

IV.B. Mean and Second order Statistics

A comparison of temporally averaged mean streamwise velocity profile and streamwise velocity contour in xz plane for two different outflow boundary conditions are shown in Figure 6. Even though, negligible discrepancies are observed for the contour plot, some differences are noted for the line plots of velocity profile in Figure 6a, 6b, but they are mainly restricted in the outer layer much above the turbine wake at $z/D \gtrapprox 2$. However, the stabilized natural outflow boundary condition[37] being more physically consistent has been used subsequently in the simulations, the statistics of which are reported.

Figure 7, 8 depicts the mean velocity statistics and second order velocity moments (streamwise variance $\overline{u'^2}$, kinematic shear stress $-\overline{u'w'}$) in an xz plane respectively where u', w' are fluctuations in the x and z direction respectively. The spanwise location of the xz plane is averaged in the y direction. The plots in the xz plane hopes to capture the complex phenomenon of "wake-impingement" effects manifesting streamwise (x) variation of flow along with the growth of the "inner layer" in the z direction (wind turbine roughly at the inner layer, $z_h = 0.2H$). The Figures (6c, 6d) clearly indicate symmetric nature of the wake diffusion in xz plane about the centerline of the wake which is at the hub-height (nacelle), at $z/D = 1$ in the time-averaged frame, and the wake-deficit can also be observed in the temporal mean contours. The wake-deficits of mean streamwise velocity $\overline{U}$ are expectedly of greater intensities in the second and third rows than in the first row of turbines as in Figure 7a due "wake impingement" effects. The wall-normal velocity $\overline{W}$ has expectedly a symmetric profile (upflux and downflux) at the top and bottom wake region at the turbine location, possibly because of the rotation effect of the blades. However, what is counter-intuitive, is the presence of a strong upflux or positive wall normal velocity in the wind turbine wakes, which grows stronger in the second row of turbines and beyond. The wind turbines are well within the atmospheric boundary layer (lower 25% of the boundary layer), and the interaction of atmospheric turbulence with rotating wind turbines are manifested by the growth of the "inner layer" (or the wind turbine array boundary layer) as observed in literatures.[53,58,59] However, the growth of "inner-layer" is not so prominently observed in the mean streamwise velocity contours as is in the second order statistics contours, e.g., the $\overline{u'^2}$ fluctuations and the kinematic shear stress -$\overline{u'w'}$. For the second order turbulent stresses/ fluctuations, it is observed that they occur mainly at or near the surface of the wakes and finally propagate/diffuse towards the core at $\sim 4D$ distances downstream of the rotors. This can be attributed to the formation of tip vortices in the near wake ($\sim 3D$ from turbine-nacelle) and finally breakdown due to inviscid instability mechanism in the far-wake region. It is also observed that $\overline{u'^2}$ (major contributor to turbulent kinetic energy) is maximum near the top wake region ($z \sim z_h + D/2$) while depicting **reduced turbulence activity** in the bottom wake region $z \sim z_h - D/2$.[28] The second order stresses are also of much larger intensity in the second and third rows than in the first row, which manifests the fact that there is supposedly a **positive correlation** between the larger velocity deficits in "wakes" and the production of higher turbulence.

The temporally averaged streamwise velocity profile (middle wind turbine, first row, $y/D = 8$) and second order stresses ($\overline{u'^2}$, $-\overline{u'w'}$) at distances $2D$, $5D$, $7D$ from the turbine nacelle are shown in Figures 9a, 9b, 9c and corroborate the contour plots as discussed above. The profiles have been compared against the experimental results of a 3×3 wind turbine array by Hamilton et al.[30] and a single wind turbine simulation / experiment by Wu et al.[19] Both the experiments have been conducted at $Re \sim O(10^5)$. The velocity profile shows reasonable match with the experiments especially in the top wake region, while the second order stresses shows decent match with the bottom wake region. The mean streamwise velocity profile (Figure 9a) shows that the maximum velocity deficit occurs at turbine rotor position $x_t/D = 0$ (not reported here), and with the expansion and diffusion of wake, the intensity of the wake deficit decreases as we go downstream of the turbine and this is also supported by the three different spanwise averaged profiles at $x_t/D = 2,\ 5,\ 7$. Furthermore, it is observed that the velocity profiles do not show any differences amongst each other at distances beyond $z/D \gtrsim 2.5$, indicating that the "inner layer" formed by the wind turbine arrays lies below $z < 2.5D$. Quite different trends are observed in streamwise velocity variance $\overline{u'^2}$ and kinematic shear stress $-\overline{u'w'}$ which shows that the peak magnitude at the "top-wake region" decreases beyond $x_t = 5D$. Also, $\overline{u'^2}$ shows less magnitude/intensity below turbines $z/D \lessapprox 0.5$, which indicates that the turbulence is suppressed below the turbines, which is in concordance with the idea that the power production in the wind turbine array is directly related to the vertical entrainment of mean kinetic energy[1,59] by turbulent shear-stress flux. The kinematic shear stress $-\overline{u'w'}$ show high positive magnitude near the top extent of the rotor ($z/D \sim 1.5$), while depicting a high negative magnitude near the bottom extent of the rotor ($z/D \sim 0.5$). This is not surprising or contradictory since, careful observation reveals that near the top extent of the rotor, we have positive streamwise velocity gradient $\partial U/\partial z$, while near the bottom extent we have negative gradients. This ensures that the turbulence production term $-\overline{u'w'}\partial U/\partial z$ is positive near wake surfaces contributing to the generation of turbulent kinetic energy. We would discuss more about turbulent production in the subsequent sections.

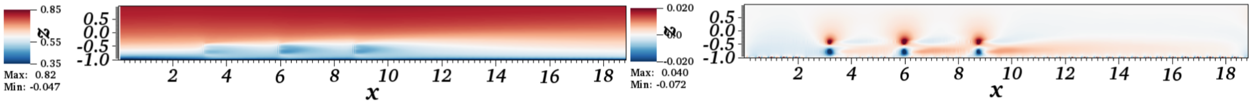

(a) (b)

Figure 7: Temporal & y averaged mean Statistics in xz plane. (a) Streamwise velocity $\overline{U}$ (b) Wall normal velocity $\overline{W}$.

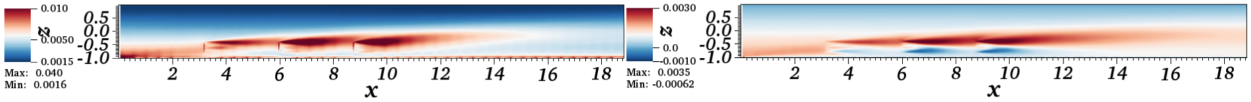

(a) (b)

Figure 8: Temporal & y averaged mean second order statistics in xz plane. (a) Streamwise variance $\overline{u'^2}$ (b) kinematic shear stress $-\overline{u'w'}$

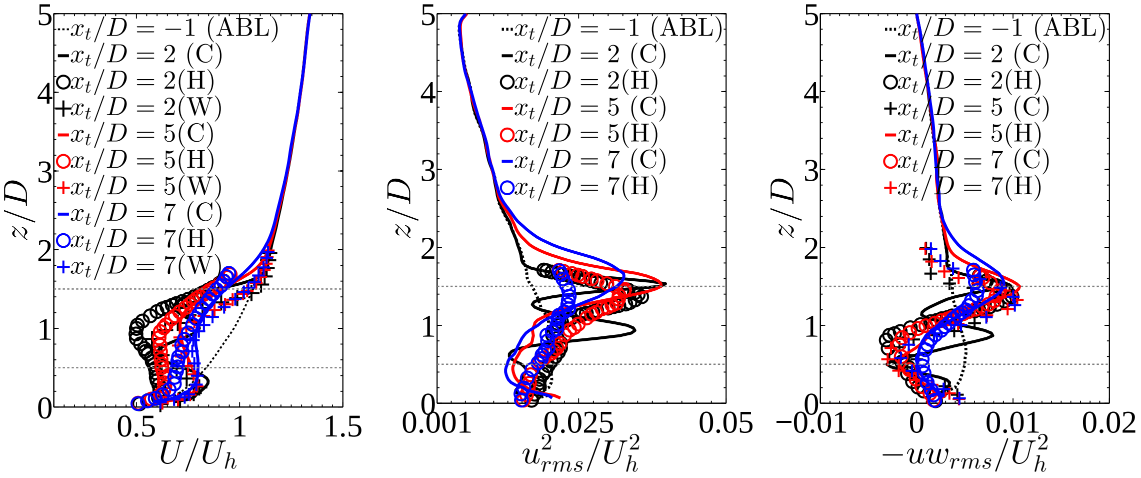

(a) (b) (c)

Figure 9: Mean streamwise (a) velocity (b) variance (c) kinematic shear stress profile at 3 different locations. $x_t = 0$: turbine-nacelle location. C is current LES simulation. Experimental results from Hamilton et. al[30] (H) and Wu et. al[19](W). Normalization by hub-height velocity U_h. Dashed lines at $z_h \pm D/2$ indicate the extent of wind turbine rotor

IV.C. Dominant Mechanisms of Wake Turbuence

To simplify our understanding on the contribution of turbulence in wakes we resort to the temporally averaged mean streamwise momentum equation. Even though the computational setup is not a periodic domain in the streamwise-spanwise direction as in WTABL, the equation is similar to a WTABL, since the growth of the boundary layer is manifested by the dominant $\partial/\partial z$ term & $O(\overline{W}) \ll O(\overline{U})$ in mean streamwise velocity equation described below. $\partial\overline{p}/\partial x$ and $\overline{F}_x$ are the mean streamwise pressure gradient and streamwise forces in the turbines respectively.

$$\frac{D\overline{U}}{Dt} = -\frac{1}{\rho}\frac{\partial\overline{p}}{\partial x} + \overline{F}_x + \frac{\partial}{\partial z}\left(\nu\frac{\partial\overline{U}}{\partial z} - \overline{u'w'}\right) \tag{11}$$

Multiplying Equation(11) with $\overline{U}$ we can recover the mean kinetic energy equation as follows

$$\frac{D\left(\frac{1}{2}\overline{U}^2\right)}{Dt} = -\frac{1}{\rho}\overline{U}\frac{\partial\overline{p}}{\partial x} + \overline{UF}_x + \overline{U}\frac{\partial}{\partial z}\left(\nu\frac{\partial\overline{U}}{\partial z} - \overline{u'w'}\right) \tag{12}$$

The turbulent contribution in the mean kinetic energy (See Equation(12)) comes from the kinematic Reynolds shear stress term $-\overline{U}\partial\overline{u'w'}/\partial z$. This term can be further broken down into

$$-\overline{U}\frac{\partial\left(\overline{u'w'}\right)}{\partial z} = -\frac{\partial}{\partial z}\left(\overline{U}\overline{u'w'}\right) - \left(-\overline{u'w'}\frac{\partial\overline{U}}{\partial z}\right) \tag{13}$$

where $-\overline{U}\overline{u'w'}$ is the turbulent flux term to the mean kinetic energy, and neglecting viscous terms ($Re \sim 10^{10}$), the turbulent diffusion of mean kinetic energy comes from $\left(-\overline{u'w'}\frac{\partial\overline{U}}{\partial z}\right)$ which incidentally adds to the production of turbulence in the turbulent kinetic energy budget. Along the lines of WTABL as seen in[1,2] it is intuitive to think from the integral of the mean kinetic energy equation over yz plane, that the power contribution from the turbine roughly comes from a fraction of the integral of $\int_{z_h-D/2}^{z_h+D/2}\left(\partial/\partial z(-\overline{U}\overline{u'w'}\right)dz$ (roughly the difference difference between the fluxes $-\overline{U}\overline{u'w'}$ at $z_h \pm D/2$), while the pressure gradients approximately balance the turbulence dissipation. This analysis provides a motivation to study the turbulent fluxes and turbulent dissipation contours in the xz plane (averaged in y direction), especially their streamwise variation as depicted in Figures 10 and see if the analysis made in the past regarding turbulent fluxes and turbulent production/ dissipation in WTABL,[2,1,30] can be meaningfully applied in an isolated 3 wind turbine array.

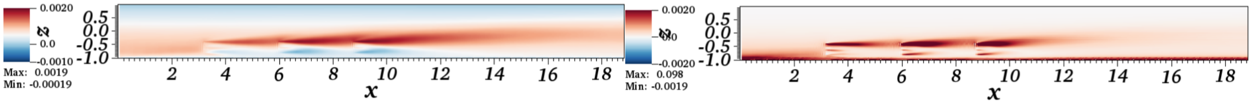

(a)

(b)

Figure 10: Temporal & y averaged mean (a) turbulent shear stress flux $-\overline{u'w'U}$ (b) turbulence production $-\overline{u'w'}d\overline{U}/dz$ in xz plane

Figures 10a, 10b shows the temporal & y averaged turbulent shear stress flux and the turbulent dissipation of the mean kinetic energy in an xz plane. The turbulent shear stress flux clearly shows an increment in the stress flux in the top wake region ($z/D \sim 1.5$), from the second row of wind turbines, but the flux at the bottom wake region ($z/D \sim 0.5$) decreases as well, justifying that the difference in the flux at $z_h \pm D/2$ increases in the second and third row of turbines than at the first row. Also, maximum peaks of the flux shift upwards justifying the growth of the inner layer. However, power calculations, as will be shown later, indicate that the power production in second and third row of turbines decreases compared to the first row, due to "wake impingement" effects. Consequently, the fraction of the flux difference which contributes to the wind power varies and possibly decreases along the streamwise direction. This is expectedly, due to the sustenance of no-zero convective terms of the kinetic energy (inner layer growth due to $D/Dt(1/2\overline{U}^2)$) in the 3×3 wind turbine array contributed from the differential shear stress flux unlike the WTABL. Hence the simple equilibrium of mean kinetic energy discussed above although serves as a good building block of a WTABL model, cannot be applied in an isolated 3×3 wind turbine array. The turbulent dissipation of mean kinetic energy, which contributes to the turbulent production term in the tke budget (Figure 10b) shows three distinct regions of high production. At $z \sim 0.1H$ or $z \sim 0.4D$, the turbulence generated is mainly "wall-bounded" in nature contributed from the anisotropic coherent structures associated with the self-sustaining mechanism of wall turbulence.[60,61] The next two regions primarily occur at $z \sim z_h \pm D/2$, with the top-wake at the outer layer having significantly higher production than the bottom-wake. At the bottom wake, kinematic shear stress $-\overline{u'w'}$ produced is slightly lower than at the top wake possibly due to near-wall effects, and mean velocity gradient $\partial\overline{U}/\partial z$ is also smaller in the velocity deficit region closer to the wall. Subsequently, it is straightforward to see that the turbulence production $-\overline{u'w'}\partial\overline{U}/\partial z$ in the bottom wake is smaller than at the top wake.

IV.D. Temporal Power Spectra

The power generated by the wind turbines is usually quantitatively represented with power coefficient C_p. Average radial forces per blade $\overline{F}_r$ (averaged over the rotor length) are computed in our simulations, from which the torque on each blade can be calculated in a straightforward manner by multiplying with the

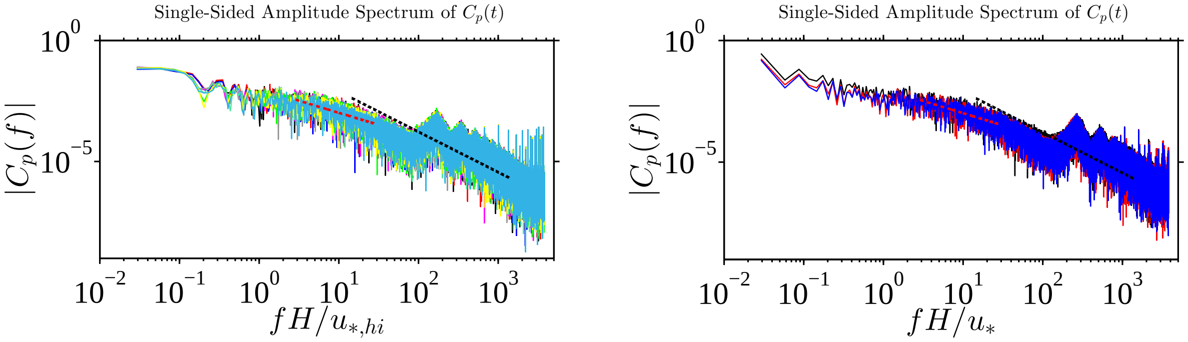

(a) (b)

Figure 11: Temporal power coefficient spectra for (a) periodic domain, WTABL, all 9 turbines (b) isolated 3×3 wind turbine array, turbines in 3 different rows at mid-plane $y/D = 8$. Black: first row, Red: second row, Blue: third row. Lines - Red-dashed: f^{-1} law; Black-dashed: $f^{-5/3}$ law.

number of blades and rotation rate of the blades.

$$C_p = \frac{\int_{R_i}^{R_o} rF_r dr \times B \times \Omega}{\frac{1}{2}\rho A U_b^3} = \frac{\overline{F}_r \times \frac{1}{2}(R_o^2 - R_i^2) \times B \times \Omega}{\frac{1}{2}\rho A U_b^3} \tag{14}$$

where R_i, R_o are the minimum and maximum radial extent of the blades ($R_i \neq 0$, due to the nacelle), $B = 3$ is the number of blades and Ω, the rotation rate of the turbine. $A = \pi(R_o^2 - R_i^2)$ is the rotor-swept area and we define U_b to be always the bulk mean velocity intercepted by the first row of wind turbines.

A comparison of the temporal spectra of the power coefficient C_p vs the normalized frequency spectra are depicted in Figure 11 (normalized with eddy turn over time H/u_*, where u_* is the friction velocity scale at the bottom wall; for periodic WTABL, $u_{*,hi}$ corresponding to the upper equilibrium log-layer is used). In Figure 11a, we indeed see that the power generated by all the wind turbines is similar to ~ 0.25 (validated by Cal et. al[2] who reported $C_p \sim 0.28$ in their studies). This is expected, since in very large wind farms, and wind conditions which yield fairly stationary statistics in time, the power generated by a small array of the turbines in the centre of the farm would be fairly constant and independent of "wake impingement" effects. In a stark contrast we observe that the "wake-impingement" effects are conspicuously seen in Figure 11b, where there is significant drop of power from second row and beyond (from $C_p \sim 0.28$ in first row middle turbine, to $C_p \sim 0.12$, last row middle turbine), due to interception of reduced momentum deficit profiles in the subsequent rows due wake generation.

Both the temporal spectra of the power coefficients clearly show a distinct f^{-1} and $f^{-5/3}$ scaling laws (validated by [62] in field experiments). In lower frequency region the frequency of the wake-meandering phenomenon can be observed at $fH/u_* \sim O(10^{-1})$ which matches with the approximate scale of $f_{wm} \sim \overline{U}/2D_w$ ($D_w \sim D$, diameter of the wake). In the higher frequency region beyond $-5/3$ law (low energy contribution), $fH/u_* \sim O(10^2)$ multiple distinct $C_p(f)$ peaks show up corresponding to the constant rotational rate of the 3 bladed turbines, $f_r = 3\Omega/(2\pi)$ and their superharmonics $2f_r, 3f_r, 4f_r$ etc with lower $C_p(f)$ peaks. This phenomenon can be conceived as the power generation by the interception of eddies with the turbine blades on a time scale much larger than $O(f_r^{-1})$, such that the eddies almost behave like a "frozen field" being intercepted by the blades. The presence of superharmonics of f_r at higher frequencies suggests a "periodic temporal coherence" at time scales of the order of rotation period $2\pi/\Omega$. The temporal power spectra plots give a clear indication that the power generated by the wind turbines are in major contributed by eddies of large or intermediate time scales ($fH/u_* < O(10^{-1})$) which can be observed in both large wind farms (periodic domains) as well as 3×3 wind turbine array. This is further corroborated in Figure 11b where conspicuous discrepancies in the power coefficient C_p among various rows of turbines can be observed only at low frequency region $fH/u_* < O(10^{-1})$ (near wake meandering frequency), beyond which the scaling laws and the high frequency superharmonics collapse on the same curve for turbines at different rows.

V. Conclusion

In the current paper, we have considered a large-eddy simulation study of a 3 × 3 wind turbine array, and its behaviour in contrast to large wind farms (periodic WTABL) are studied. We have observed that in such short length-scale wind farms, important phenomenon like the growth of the "inner layer" due to wake expansion, "wake impingement" effects on subsequent turbine rows play an important role in power generation which are not observed in the simplified WTABL model of power generation. In particular by studying the second order turbulent stresses, we have concluded that the dynamics of the turbines in the second row and beyond are grossly different from the first row of turbines which intercept atmospheric flows. In the subsequent rows, the mean velocity wake-deficits and turbulent stresses are stronger, especially in the top wake surface and the large-scale turbulent mechanisms have an increasing dominant contribution to the wake turbulence production. Finally the temporal power spectra of the 3 × 3 wind turbine arrays justifies the contribution of large-scale eddies that play a major role in "wake-impingement" and hence the reduction in power generation in the second and third row of wind turbines.

The future work would involve studies considering larger arrays of wind turbines with inflow-outflow boundary condition and observe if they behave similar to periodic WTABL as in large wind farms. Also, we plan to couple realistic field experimental results with our LES model using Data Assimilation techniques, to generate fine scale realistic flows to drive wind turbine arrays in an effort to better predict the power generated by the wind turbines.

VI. Acknowledgements

The authors would like to acknowledge the support of NSF-CBET 13358568 grant for the present work. The authors would also like to thank Dr. Oana Marin, Argonne National Laboratory, for some expert guidance regarding outflow boundary conditions.

References

[1] Calaf, M., Meneveau, C., and Meyers, J., "Large Eddy Simulation Study of Fully Developed Wind-Turbine Array Boundary Layers," *Phys. Fluids*, Vol. 22, 2010, pp. 015110.

[2] Cal, R. B., Lebron, J., Kang, H. S., Castillo, L., and Meneveau, C., "Experimental study of the horizontally averaged flow structure in a model wind-turbine array boundary layer," *J. Renewable and Sustainable Energy*, Vol. 2, 2010, pp. 013106.

[3] Chatterjee, T. and Peet, Y., "Spectra and Large Eddy Structures in the double log-layer of a high Re Wind Turbine Array Boundary Layer," Proceedings of ASME Turbo Expo 2016: Turbomachinery Technical Conference and Exposition GT2016-56359, 2016, (submitted).

[4] Frandsen, S., ans S. Pryor, R. B., Rathmann, O., Larsen, S., Hojstrup, J., and Thogersen, M., "Analytical modelling of wind speed decit in large offshore wind farms," *Wind Energy*, Vol. 9, 2006.

[5] Meyers, J. and Meneaveau, C., "Large Eddy Simulations of large wind-turbine arrays in the atmospheric boundary layer," AIAA paper 2010–827, 2010, 4 - 7 January 2010, Orlando, Florida.

[6] Pope, S. B., *Turbulent Flows*, Cambridge Press, 2000.

[7] Piomelli, U. and Balaras, E., "Wall-layer models for large eddy simulations," *Annu Rev. Fluid. Mech*, Vol. 34, 2002, pp. 349–374.

[8] Reynolds, W. C., "The potential and limitations of direct and large eddy simulations," *Lecture Notes in Physics*, Vol. 357, J. L. Lumley, Ed., Springer-Verlag, Berlin, 1990, pp. 313–343.

[9] Friedrich, R. and Unger, F., "Large eddy simulation of boundary layers with a step change in pressure gradient," *J. Fluid. Mech.*, Vol. 41, 1970, pp. 453–480.

[10] Piomelli, U., "Large eddy simulation: achievements and challenges," *Prog. Aerospace Sci.*, Vol. 35, 1999, pp. 335–62.

[11] Piomelli, U., "High Reynolds number calculation using the dynamic subgrid-scale stress model," *Phys. Fluids A*, Vol. 5, 1993, pp. 14–84.

[12] Porté-Agel, F., Meneveau, C., and Parlange, M. B., "A scale-dependant dynamic model for large eddy simulation: application to a neutral atmospheric boundary layer," *J. Fluid. Mech.*, Vol. 17, 2000, pp. 261–284.

[13] Deardorff, J. W., "A numerical study of three-dimensional turbulent channel flow at large Reynolds number," *J. Fluid. Mech.*, Vol. 41, 1970, pp. 453–480.

[14] Schumann, U., "Subgrid scale model for finite difference simulations of turbulent flows in plane channels and annuli," *J. Comp. Phys.*, Vol. 18, 1975, pp. 376–404.

[15] Germano, M., Piomelli, U., Moin, P., and Cabot, W. L., "A dynamic subgrid-scale eddy viscosity model," *Phys. Fluids,A*, Vol. 3, 1991, pp. 1760–1765.

[16] Moeng, C. H., "A large eddy simulation model for the study of planetary boundary-layer turbulence," *J. Atmos. Sci.*, Vol. 46, 1984, pp. 2311–2330.

[17] Ivanell, S. S. A., *Numerical Computations of Wind Turbine Wakes*, Ph.D. thesis, Dept. of Mechanics, Gotland Univ., Stockholm, Sweden, 2010.

[18] Troldborg, N., *Actuator Line Modeling of Wind Turbine Wakes*, Ph.D. thesis, Technical University of Denmark, 2008.

[19] Wu, Y.-T. and Porté-Agel, F., "Large-Eddy Simulation of Wind-Turbine Wakes: Evaluation of Turbine Parametrisations," *Boundary Layer Metereol*, Vol. 138, 2011, pp. 345–366.

[20] Chatterjee, T. and Peet, Y., "Actuator Line Wind Turbine Simulations in Atmospheric Turbulent Flows using Spectral Element Method," AIAA paper 2015–0727, 2015, 05 - 19 January 2015, Kissimmee, Florida.

[21] Merrill, B. and Peet, Y., "High-Order Moving Overlapping Grid Methodology for Aerospace Applications," AIAA paper 2015–1743, 2015, 05 - 19 January 2015, Kissimmee, Florida.

[22] Rankine, W. J. M., "On the Mechanical Principles of the Action of Propellers." *Trans. Inst. Naval Architects*, Vol. 6, 1865.

[23] Glauert, H., "Airplane Propellers," *Aerodynamic Theory*, ed. W. F. Durand, New York 4, Div. L, 1963, pp. 128–143.

[24] Sørensen, J. N. and Myken, A., "Unsteady actuator disc model for horizontal axis wind turbines," *J. of Wind Eng. and Ind. Aerodynamics*, Vol. 39, 1992, pp. 139–149.

[25] Sørensen, J. N. and Shen, W. Z., "Numerical modelling of Wind Turbine Wakes," *J. Fluids Eng.*, Vol. 124, 2002, pp. 393–399.

[26] Peet, Y., Fischer, P., Conzelmann, G., and Kotamarthi, V., "Actuator Line Aerodynamics model with Spectral Elements," AIAA paper 2013–1210, 2013, 07 - 10 January 2013, Grapevine (Dallas/Ft. Worth Region), Texas.

[27] Porté-Agel, F., Wu, Y.-T., and Conzemius, R. J., "Large-Eddy Simulation of Atmospheric Boundary Layer Flow Through Wind Turbines and Wind Farms," *J. of Wind Eng. and Ind. Aerodynamics*, Vol. 99, 2011, pp. 154–168.

[28] Churchfield, M. J., Michalakes, J., and Moriarty, P. J., "A Numerical Study of the Effects of Atmospheric and Wake Turbulence on Wind Turbine Dynamics,," *J. Turb.*, Vol. 13, No. 14, 2012, pp. 1–32.

[29] Churchfield, M. J., , Moriarty, P. J., Hao, Y., Lackner, M., Berthelmie, R., Lundquist, J. K., and Oxley, G. S., "A Comparison of Dynamic Wake Meandering Model, Large Eddy Simulation and Field Data at the Egmond aan Zee Offshore Wind Plant," AIAA Paper 2015-0724, 2012.

[30] Hamilton, N., Kang, H. S., Meneveau, C., and Cal, R. B., "Statistical analysis of kinetic energy entrainment in a model wind turbine array boundary layer," *J. Renewable and Sustainable Energy*, Vol. 4, 2012, pp. 063105.

[31] Lebrón, J., Castillo, L., Cal, R. B., Kang, H. S., and Meneaveau, C., "Interaction between a wind turbine array and a turbulent boundary layer," AIAA paper 2010-824, 2010, 4 - 7 January 2010, Orlando, Florida.

[32] Spalart, P. R., "Direct Simulation of turbulent boundary layer up to $Re_\theta = 1400$," *J. Fluid. Mech.*, Vol. 187, 1988, pp. 61–98.

[33] Lund, T. S., Wu, X., and Squires, K. D., "Generation of turbulent Inflow data for Spatially-Developing Boundary Layer Simulations," *J. Comp. Physics*, Vol. 140, 1998, pp. 233–258.

[34] Ferrante, A. and Elghobashi, S. E., "A robust method for generating inflow conditions for direct simulations of spatially developing turbulent boundary layers," *J. Comp. Physics*, Vol. 198, 2004, pp. 372–387.

[35] Colonius, T., "Modeling artificial boundary conditions for compressible flow," *Annu. Rev. Fluid. Mech.*, Vol. 36, 2004, pp. 315–345.

[36] Walchshofer, C., Steiner, H., and Brenn, G., "Robust Outflow Boundary Conditions for Strongly Buoyant Turbulent Jet Flames," *In:Flow, Turbulence and Combustion*, Vol. 86.3-4, 2010, pp. 713–734.

[37] Dong, S., Karniadakis, G., , and Chryssostomidis, C., "A robust and accurate outflow boundary condition for incompressible flow simulations on severely- truncated unbounded domains," *J. Comput. Physics.*, 2010.

[38] Meneveau, C., "Wind turbine array fluid dynamics: measurement and modelling," 2009, http://cfd.mae.cornell.edu/caughey/.

[39] Schlatter, P., Adams, N. A., and Kleiser, L., "A windowing method for periodic inflow/outflow boundary treatment of non-periodic flows," *J. Comput. Physics.*, Vol. 206, 2005, pp. 505–535.

[40] Stoll, R. and Porté-Agel, F., "Dynamic subgrid-scale models for momentum and scalar fluxes in large-eddy simulations of neutrally stratified atmospheric boundary layers over heterogeneous terrain," *Water Resources Research*, Vol. 42, 2006, pp. W01409.

[41] Fischer, P. F., Lottes, J. W., and Kerkemeier, S. G., "nek5000 Web page," 2008, http://nek5000.mcs.anl.gov.

[42] Fischer, P., "An Overlapping Schwarz Method for Spectral Element Solution of the Incompressible NavierStokes Equations," *J. Comp. Phys.*, Vol. 133, 1997, pp. 84–101.

[43] Fischer, P., Lottes, J., Pointer, D., and Siegel, A., "Petascale Algorithms for Reactor Hydrodynamics,," *J. Phys. Conf. Series*, 2008.

[44] Deville, M. O., Fischer, P. F., and Mund, E. H., *High-Order Methods for Incompressible Fluid Flow*, Cambridge University Press, Cambridge, UK, 2002.

[45] Orszag, S. A., "Transform method for calculations of vector coupled sums: Application to the spectral form of vorticity equation," *J. Atmos. Sci.*, Vol. 27, 1970, pp. 890–895.

[46] Canuto, C. M., Hussaini, Y., Qaurteroni, A., and Zhang, T. A., *Spectral Methods in Fluid Dyanamics*, New York: Springer, 8th ed., 1988.

[47] Mason, P. J. and Thompson, D. J., "Stochastic backscatter in large-eddy simulations of boundary layers," *J. Fluid. Mech.*, Vol. 242, 1992, pp. 51–78.

[48] Monin, A. S. and Obukhov, A. M., "Basic Laws of Turbulent Mixing in the Ground Layer of the Atmosphere," *Trans. Geophys. Inst. Akad. Nauk. USSR*, Vol. 151, 1954, pp. 163–187.

[49] Meneaveau, C. and Katz, J., "Scale-invariance and turbulence models for large eddy simulation of boundary layers," *Ann. Rev. Fluid. Mech.*, Vol. 32, 2000, pp. 1–32.

[50] Wu, P. and Meyers, J., "A constraint for subgrid-scale stresses in the logarithmic region of high Reynolds number turbulent boundary layers: A solution to log-layer mismatch problem," *Phys. Fluids*, Vol. 25, 2013, pp. 015104.

[51] Boström, E., "Investigation of Outflow Boundary Conditions for Convection-Dominated Incompressible Fluid Flows in a Spectral Element Framework," 2015, Master's Thesis, KTH, Sweden.

[52] Mikkelsen, R., *Actuator Disc Methods Applied to Wind Turbines*, Ph.D. thesis, Technical University of Denmark, 2003.

[53] Churchfield, M. J., Lee, S., Moriarty, P. J., Martinez, L. A., Leonardi, S., Vijayakumar, G., and Brasseur, J. G., "A Large-Eddy Simulation of Wind-Plant Aerodynamics," AIAA Paper 2012-0537, 2012.

[54] Fischer, P. and Mullen, J., "Filter-based stabilization of spectral element methods," *Comptes rendus de lAcadémie des sciences, Série I- Analyse numérique*, Vol. 332, 2001, pp. 265–270.

[55] Perry, A. E., Henbest, S., and Chong, M. S., "Theoretical and Experimental studies of wall turbulence," *J. Fluid. Mech.*, Vol. 165, 1986, pp. 163–199.

[56] Nickels, T. B., Marusic, I., Hafez, S., Hutchins, N., and Chong, M. S., "Some Predictions of the Attached Eddy Model for a High Reynolds Number Boundary Layer," *Phil. Trans. R. Soc.*, Vol. 365, 2007, pp. 807–822.

[57] Bou-Zeid, E., Meneveau, C., and Parlange, M., "A scale-dependant Lagrangian dynamic model for large eddy simulation of complex turbulent flows," *Phys. Fluids*, Vol. 415, 2005, pp. 025125.

[58] Stevens, R. J. A. M., Gayme, D., and Meneveau, C., "Coupled Wake Boundary Layer Model fo Wind Farms," *Journal of Renewable and Sustainable Energy (accepted)*, 2015.

[59] Allaerts, D. and Meyers, J., "Large eddy simulation of a large wind-turbine array in conventionally neutral atmospheric boundary layer," *Phys. Fluids*, Vol. 27, 2015, pp. 065108.

[60] Jiménez, J., "On a self-sustaining process in shear flows," *Phys. Fluids.*, Vol. 9, 1997, pp. 883.

[61] Jiménez, J., "Cascades in Wall Bounded Turbulence," *Annu. Rev. Fluid. Mech.*, Vol. 44, 2012, pp. 27–45.

[62] Apt, J., "The spectrum of power from wind turbines," *J. Power Sources*, Vol. 169, 2007, pp. 369–374.